A quantitative study of moisture transport variation on the interdecadal variation of the summer precipitation in South China from 1979 to 2015

Linhao Zhong[1,2] · **Lijuan Hua**[3] · **Zhuguo Ma**[1] · **Yao Yao**[1]

Abstract

The summer precipitation in South China (SC) has experienced a pronounced interdecadal variation during 1983–2013 with trend transition in the late 1990s. This study quantitatively investigates the precipitation variation and its connection to water vapor transport by combining the Lagrangian trajectory-based Dynamic Recycling Model and the clustering method of self-organizing map. The external moisture outside of SC explains most (84%) of the mean and the interdecadal variation of the summer rainfall, mainly through the southwest transport pathways. A long-distance southwest pathway related to cross-equatorial flow and eastward flow over the Northern Indian Ocean explains 31.5% of mean precipitation and 50.4% of the upward precipitation trend before 1997. The other branch of the southwest pathways has relatively shorter length over North Indian Ocean, South China Sea, and Southeast Asia, explaining 35.7% of the mean and 51.2% of the downward trend after 1997. Also, for the downward trend, the westerly-driven moisture transport over Eurasia acts as the second contributor (32.2%) to the precipitation decrease. However, the western-Pacific pathway explains the smallest portion ($\leq 3\%$) of the trends, suggesting weak influence from the subtropical high. The large-scale circulation anomaly in the form of zonal and meridional wave trains control the interdecadal variability of the SC precipitation. It is found that the circumglobal teleconnection and Pacific–Japan teleconnection significantly correlate to the two wave trains, whose match relation strongly modulates the trend transition in the 1990s for the SC summer precipitation.

Keywords South China · Interdecadal precipitation variation · Moisture transport · Wave train · Dynamic Recycling Model · Self-organizing map

1 Introduction

The long-term changes of precipitation are of vital importance for the regional societal and economic development (Yao et al. 2008; Wu et al. 2010). The variabilities of precipitation over East Asia have been studied in depth (Gong and Ho 2002; Hsu and Lin 2007; Ding et al. 2008; Li and Leung 2013; Wei et al. 2012). Many studies have investigated the temporal and spatial variation of the precipitation over Asia as well as that over China. Among these researches, the abrupt precipitation shifts in the late 1970s (Hu 1997; Ding et al. 2009; Sun and Wang 2012) and the middle of the 1990s (Kwon et al. 2007; Ding et al. 2008; Yao et al. 2008; Si et al. 2009) are the frequently studied topics. Multiple factors have been presented to explain the decadal or interdecadal precipitation regime shifts in East Asia (Hu 1997; Gong and Ho 2002; Yao et al. 2008; Ding et al. 2009; Si et al. 2009; Wu et al. 2010; Jin et al. 2016). In East Asia, it is unquestionable that the summer monsoon dramatically shapes the precipitation pattern and its long-term variation in East Asia for the late-1970s transition, through the El Niño and South Oscillation (ENSO) related modes (Wang 2002; Gao et al. 2006). However, earlier analysis

✉ Linhao Zhong
zlh@mail.iap.ac.cn

✉ Lijuan Hua
hualj@ucas.ac.cn

1 CAS Key Laboratory of Regional Climate-Environment for Temperate East Asia, Institute of Atmospheric Physics, Chinese Academy of Sciences, Beijing, China

2 Laboratory for Regional Oceanography and Numerical Modeling, Qingdao National Laboratory for Marine Science and Technology, Qingdao, China

3 Key Laboratory of Computational Geodynamics, University of Chinese Academy of Sciences, Beijing, China

(Simmonds et al. 1996) emphasized the role of the Western-Pacific 'warm pool' in the multidecadal variability of the summer rainfall in China but without finding a strong synchronous connection between the Southern Oscillation Index and summer precipitation in China. Moreover, focusing on the precipitation transition in 1990s, recent studies suggest decadal variability related to several other climatic modes should also be emphasized, such as the decadal shifts of the East Asia–Pacific/Pacific Japan (EAP/PJ) teleconnection (Yu et al. 2012; Chen and Zhou 2014), the western North Pacific (WNP) summer monsoon-related mode (Kwon et al. 2005), the summer North Atlantic Oscillation (NAO) (Sun and Wang 2012) and the warming over the Tibetan Plateau (Si et al. 2009; Si and Ding 2013).

The shift of Asian summer monsoon (Wang 2001) leads to rainfall pattern of "southern flood and northern drought" in East China. Since the end of the 1970s, northward moisture transport has been dramatically decreased associated with the weakening of the East Asian summer monsoon (EASM) (Ding et al. 2008), whose impact factors include the changes of major atmospheric and oceanic patterns in the Tropics (such as ENSO, interdecadal Pacific oscillation), middle/tropical to high latitudes (such as NAO, Arctic Oscillation, PJ, the Silk Road pattern and East Asian subtropical westerly jet), the sensible heat source over the Tibetan Plateau and the aerosol forcing, even sea ice concentration over the Arctic (Hsu and Lin 2007; Ding et al. 2009; Zhou et al. 2009; Si and Ding 2013; Wu et al. 2009; Li and Leung 2013). Thus, the precipitation variability in East China seems to be attributable to the cooperative formation mechanism between middle-to-high-latitude and tropical systems.

On the other hand, from the perspective of the water vapor transport, the change of transport pathways may directly result in the precipitation variation although the water vapor transport cannot tell the whole story of regional precipitation. The convergence of water vapor flux was reported to be more intimately related to the precipitation, just as some previous work has shown (Simmonds et al. 1999). However, here, we are more concerned with the impact of the variation of the moisture source as well as its transport pathway because the convergent water vapor leading to regional precipitation is contributed by moisture sources. Fundamentally, the variation of moisture source modulates the precipitation change through related physical processes, such as the water vapor convergence by atmospheric circulation. Therefore, it is especially helpful for the understanding of the dominant physical processes of the precipitation variability through quantitatively investigating the variation of the moisture-source contribution and the associated change of transport pathways. As was shown by Simmonds et al. (1999), the interannual variations of rainfall in the south and north parts of East China are greatly influenced by the monsoon circulations and the mid-latitude westerlies, respectively.

Furthermore, at decadal timescale, the precipitation variations over East China has been found to be related to the changes in water vapor transport from the external sources but not the precipitation recycling processes, i.e., precipitation contributed by the local evaporation (Huang et al. 1998; Zhou et al. 2008; Wei et al. 2012; Hua et al. 2017a). Although the increased water vapor transport from the adjacent oceans and the mid-latitude westerly transport favor precipitation over East China (Zou et al. 2010; Ma et al. 2017), the origins of water vapor related to anomalous rainfall patterns in East China are different from those related to the monsoon rainfall (Zhou and Yu 2005). This discrepancy still needs further investigation on the variations of the moisture sources. However, the comprehensive understanding of the quantitative contribution of the moisture sources responsible for the rainfall variation is still absent in East China. Ding et al. (2008) suggested that there existed two significant transitions of summer precipitation in East China, one occurring at the end of the 1970s across the whole region of East China while the other appearing in 1990s mainly in South China (SC, the south region to Yangtze River Valley), which is the southeast part of East China. Recent effort (Jiang et al. 2017) has provided a quantitative estimation of moisture source contribution to the precipitation transition in the late 1970s in the north part of East China. However, for the inhomogeneous precipitation variation in the 1990s in East China, particularly for the precipitation transition in 1990s in SC, the anomalous moisture source and transport causing the precipitation change are still unclear.

The precipitation in SC is simultaneously influenced by westerlies and East Asian Monsoon. The moisture sources and transport pathways of SC experience considerable seasonal variation that is regulated by multiple circulation systems. Therefore, this nature of the climate systems is very complicated and uncertain (Gimeno et al. 2012), making it a difficult work to identify the moisture origins from remote source regions by moisture flux estimates (Wei et al. 2012). Therefore, the Lagrangian method based on the water vapor back trajectories became a better choice to tracing water vapor trajectories and identifying sources across global and regional scales (Dirmeyer and Brubaker 1999; Stohl and James 2004; Sodemann et al. 2008; Gimeno et al. 2012; Knoche and Kunstmann 2013; Hu and Dominguez 2015; Hua et al. 2017b; Jiang et al. 2017).

With the above consideration, this study aims to quantitatively track the main evaporative moisture sources of precipitation over SC and study the possible reasons for its interdecadal transition of precipitation at the end of the 1990s. The previous study (Wang and Paegle 1996) has shown that the variations in moisture flux are much more sensitive to the variations in the wind than the variations in water vapor, which implies the critical role of the atmospheric circulation in moisture transport. So, this work also makes a particular

effort on the linkage between the atmospheric circulation and the variation of atmospheric moisture transport. To do this, a quantitative hydrological tool, i.e., the spatially unbounded Dynamic Recycling Model (DRM), which was developed by Dominguez et al. (2006) and extended by Hua et al. (2017b), is used to identify the moisture contribution and transport for the precipitation in SC.

In the sections below, we will answer the following questions quantitatively: What source regions are the most important for the mean state of the summer (June through August, JJA) precipitation over SC? What are the primary moisture pathways for the SC precipitation? Moreover, what are the roles of the primary pathways play in the precipitation interdecadal variation over SC? To do this, we organize the article as follows: Sect. 2 describes the data and methods applied in this work. The analysis results, including the quantitative estimations of the moisture transport and contribution to the SC summer precipitation, as well as the associated circulation, are presented in Sect. 3. At the end of the paper, we present a discussion and conclusion in Sect. 4.

2 Data and method

2.1 Data

In this study, three precipitation datasets covering the period of 1979–2015 are applied. Among them, the station data including 142 gauge records in SC were derived from the observation archives by the China Meteorological Administration. The distribution of the gauges is shown in Fig. 1a. In addition, another gridded observed monthly precipitation data with a spatial resolution of $1° \times 1°$ are obtained from the Global Precipitation Climatology Centre (GPCC) (Schneider et al. 2015).

The source-receptor analysis has been suffering from the lack of observational data for a long time. This study attempts to establish the source-receptor relationship for the SC precipitation by the use of the extended DRM, which is one of the analytical hydrological models in the Lagrangian frame. Because the physical basis of this model is the water vapor budget equation, the model needs a complete set of long-term and globally gridded data of the components in the water vapor equation, including precipitation, evaporation, water vapor content and water vapor flux. Unfortunately, the available observations associated hydrological cycle cannot adequately characterize budgets of water vapor because too many of the fundamental processes are missing (Gimeno et al. 2012). On the one hand, some variables necessary to the hydrological model lack of long-term observations so far. On the other hand, high uncertainty exists in the observation estimates of the main hydrological variables, particularly in precipitation and evaporation

(Wang and Dickinson 2012; Gimeno et al. 2012). So, the proxy data, such as that from numerical model simulation or high-quality reanalysis that provides complete information of hydrological cycle, becomes a common choice for many quantitative studies of source-receptor relationship (Dominguez et al. 2006; Van der Ent et al. 2010; Wei et al. 2012; Drumond et al. 2011; Keys et al. 2012; de Vries et al. 2016; Dominguez et al. 2016). These previous researches have acquired valuable knowledge on global and regional water cycles based on the proxy data. The high spatial and temporal resolution of reanalysis data can effectively compensate for the lack of direct observations.

Thus, due to the incompleteness of the observations for the quantitative estimation of the hydrologic cycle, the hydrological data obtained from the ERA-Interim (ERAI) reanalysis, which is produced by a 4DVAR assimilation system spanning from 1979 to date (Dee et al. 2011), is used as a primary data in this work. The variables utilized here include daily accumulated precipitation and evaporation that are calculated based on the ERAI 3-h forecast fields, and vertically integrated water vapor (VIWV), vertically integrated eastward and northward water vapor flux from the analysis fields at 6-h interval. The ERAI data obtained from the ECMWF online data server at a $1° \times °$ latitude–longitude resolution. In this work, the ERAI data is imported into a spatially unbounded Dynamic Recycling Model (Dominguez et al. 2006; Hua et al. 2017b) to backward track water vapor trajectories in time and identify precipitation sources, as well as their quantitative moisture contributions to the study region. The normalized departure of precipitation percentage was calculated, which can reflect the moisture surplus/deficit induced by precipitation anomaly (Zhang and Zhou 2015). Also, the vertically integrated horizontal water vapor flux and 500-hPa geopotential height (Z500) are used to produce the relevant features of the large-scale atmospheric circulation associated with the change of the SC precipitation.

To be frankly, we should use the reanalysis data in the hydrological analysis with great caution because of the uncertainties of surface moisture fluxes introduced by numerical errors, assimilation scheme, and observation system and the possible violation of the freshwater cycle caused by data assimilation (Kalnay et al. 1996; Trenberth et al. 2011). Previous work has reported that ERA-Interim reanalysis has the bias of overestimating the rainfall in most of the Northern Hemisphere with compared to GPCC (Dee et al. 2011). From the more regional evaluation, Liu et al. (2018) found the spatiotemporal performances of ERA-Interim precipitation are statistically acceptable in East China (including SC) although ERA-Interim also has higher precipitation amounts relative to station observation. Over the most area of SC, their results further showed that the ERA-Interim precipitation has no statistically significant differences in annual and seasonal means with

Fig. 1 The map of South China (SC) and its summer precipitation variation during 1979–2015: **a** the study region (black-line box) and the spatial distribution of 142 gauge stations in it (solid dots), where the color shading indicates the terrestrial and oceanic topography; **b** normalized monthly time series of the regional means of anomalous summer precipitation percentage from gauge station observations (black solid line), GPCC data (red solid line) and ERAI data (green solid line) over SC from 1979 to 2015. The straight solid thick lines in **b** show the linear trends during the two sub-periods (1983–1997, T1 and 1998–2013, T2). The linear trend slopes (decade^{-1}) of the two sub-periods are shown in the bottom of the figure, where the symbol ** represents the Mann–Kendall test at the significance level of $p < 0.05$
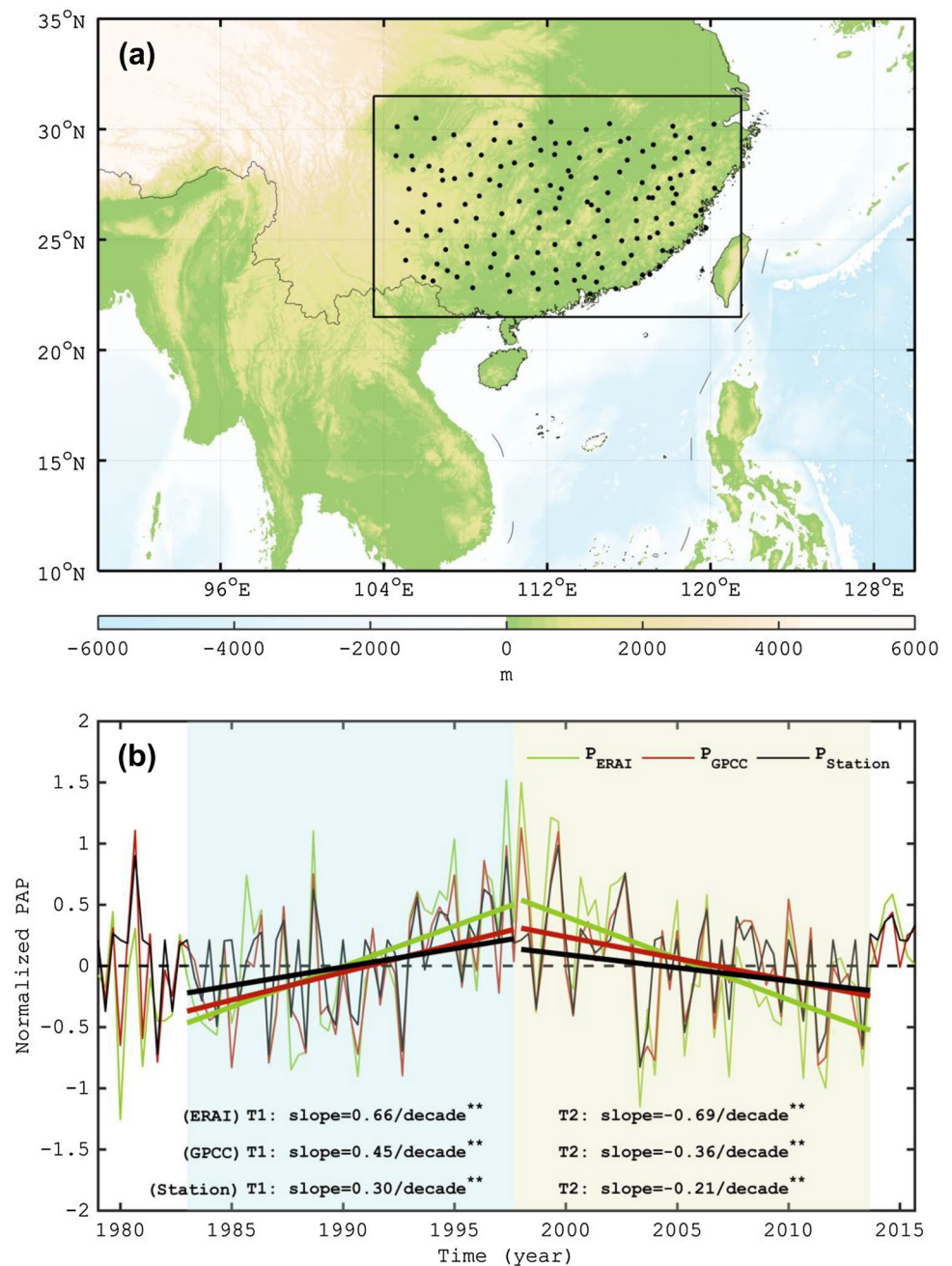
compared to the ground station observation. The dense observations available in SC lead to much weaker bias and higher skill score in East China than west of China. In addition, ERA-Interim precipitation also presents comparable trends with station precipitation for annual and seasonal means (Liu et al. 2018). Overall, the ERA-Interim precipitation has good agreement with the ground station in east China with an elevation lower than 1000 m (Liu et al. 2018). The area of SC studied by our work is just located in that acceptable area where ERA-interim precipitation shows high performance.

For the evaporation over China, Su et al. (2015) assessed most popular reanalysis datasets, including NCEP I, NCEP II, MERRA, JRA-55, and ERA-Interim. The reference data they used to evaluate reanalysis is the actual evapotranspiration (AE) estimated by the Budyko equation through combing station precipitation and pan evaporation (PE). Without considering the uncertainty of AE, all the reanalysis evaporations (REs) reasonably reproduce the spatial pattern of AE over China although REs also overestimate the evaporation of SC (Su et al. 2015). In addition, all five REs show consistent variations with PE in east China. Especially, the evaporation from ERA-Interim reanalysis shows the highest

correlation with PE in SC. Thereby, for the quantitative analysis of the hydrological cycle in SC, the reanalysis almost provides the highest level of reliability with compared to other available data.

2.2 Quantitative estimation of the moisture transport

Analytical water cycle model, such as DRM, is an effective tool to establish the quantitative source-receptor relationship for a specific region (Gimeno et al. 2012). Here, the spatially unbounded DRM is applied to the SC precipitation to identify moisture sources and transport pathways at daily timescale. The detailed description of the method used here can be found in the work of Hua et al. (2017b). The original DRM is a simple two-dimensional semi-analytical Lagrangian model based on the general atmospheric water balance equation (Dominguez et al. 2006). This model can be applied to examine the precipitation recycling ratio through track back-in-time trajectory within the target region at the daily timescale. The spatially unbounded DRM is a natural extension of the regional one. The spatially unbounded DRM can be used to estimate the moisture contributions from any sources without the spatial restrictions (Hua et al. 2017b). The idea of the unbounded DRM used here is similar to that presented by Martinez and Dominguez (2014) but employs a fixed time length by setting time "boundary" to terminate the Lagrangian backward tracking of the moisture trajectory. On average, the time that water vapor resides in the atmosphere is about 10 days (Numaguti 1999). So, in many cases, the time of moisture staying in the air certainly exceeds this mean value. That suggests the backward trajectories shorter than 10 days are possibly unable to attribute an adequate ratio of the total precipitation to a source region for a water cycle study. For the Antarctic area, Sodemann and Stohl (2009) used a 20-day trajectory to identify the moisture sources by a Lagrangian method. They concluded that 10 days (~ 80% attributed) is an acceptable time scale for backward moisture tracing and a threshold scale exists at about 15 days, above which the attributed precipitation reaches a relatively steady percentage (~ 90%) (Sodemann and Stohl 2009). The portion of the attributed precipitation varies in different regions and depends on the moisture content and wind strength of the main transport pathway. Keys et al. (2012) defined the boundary of precipitation shed as 70% contribution, which is an acceptable threshold percentage for most parts of the world. Therefore, to reduce the possibility of the biased result caused by the timescale of trajectory, we implement 15-day backward moisture tracking for each grid point of SC in this study. The moisture tracing at this long timescale is conducive to capture characteristics of long-range transport and can thereby guarantee the representation of the moisture transport. Although a longer timescale of particle tracing may introduce more uncertainties in moisture trajectories, this kind of uncertainties can be effectively reduced by averaging a large number of trajectory samples (Sodemann and Stohl 2009). In this analysis, there are more than 400,000 trajectories (135 particles × 92 days per summer × 37 summers) identified from 1979 to 2015 for SC (Fig. 2a). Furthermore, the 15-day moisture trajectories averagely attribute ~ 76% of the summer precipitation in SC. With this reliable representation of the moisture state and variation of the target region, the primary moisture pathways and quantitative moisture contribution can thereby be quantitatively estimated.

2.3 Trajectory clustering through the self-organizing map

In order to obtain the primary pathways of moisture transport, the clustering technique of the self-organizing map (SOM) is used to produce the water vapor trajectories clusters. The SOM is known as an effective method for feature extraction and classification based on an unsupervised neural network (Kohonen 1982, 1998). Unlike the traditional linear reduction method, such as principal component analysis (PCA), SOM can map nonlinear high-dimensional input data onto a two-dimensional space while the topological relationships between the input data are preserved (Liu et al. 2006b), which endows SOM the ability to isolate the nonlinear structure that can be invisible to linear technique (Cavazos et al. 2002). As a clustering and pattern recognition method, the SOM was introduced to the research of meteorology and climate since around 2000 (Cavazos 2000). The previous applications of SOM have shown that it is a useful tool to extract the feature of the meteorological and climatological pattern, such as sea surface temperature (SST) and wind pattern (Risien et al. 2004; Liu et al. 2006a).

The SOM projects the input data onto a 2D regular low-dimensional grid consisting of a set of neural network units. Each unit has a weight vector $\mathbf{m} = [m_1, \ldots, m_K]$, where K is the dimension of the input data. The SOM training process is implemented through iterative algorithms. The sequential training scheme is one of the popular algorithms. In the sequential training process, the algorithm is to find the 'winner' unit whose weight vector is closest to the input vector $\mathbf{x}$ through (Vesanto et al. 2000)

$$\mathbf{x} - \mathbf{m}_c = \min_i \left\{ \mathbf{x} - \mathbf{m}_i \right\}, \tag{1}$$

where the operator $\|\cdot\|$ is the distance measure, commonly Euclidian distance, $\mathbf{m}_c$ is called the Best-Matching Unit (BMU), i.e., the winner unit, i the index of the map units. Then, the map unit is updated according to the learning rule:

$$\mathbf{m}_i(t + 1) = \mathbf{m}_i(t) + \alpha(t) h_{ci}(t) \left[\mathbf{x}(t) - \mathbf{m}_i(t) \right], \tag{2}$$

Fig. 2 The moisture trajectories of South China (SC) during June of 2002: **a** the overall trajectories; **b–e** the sets (SOM1–4) of trajectories projected by SOM. The moisture trajectories are traced by the spatially unbounded DRM. The color of trajectory represents the percentage of the accumulated moisture contribution. The black circle marks the ending point of the backward trajectory

(a)

(b)   (c)

(d)   (e)
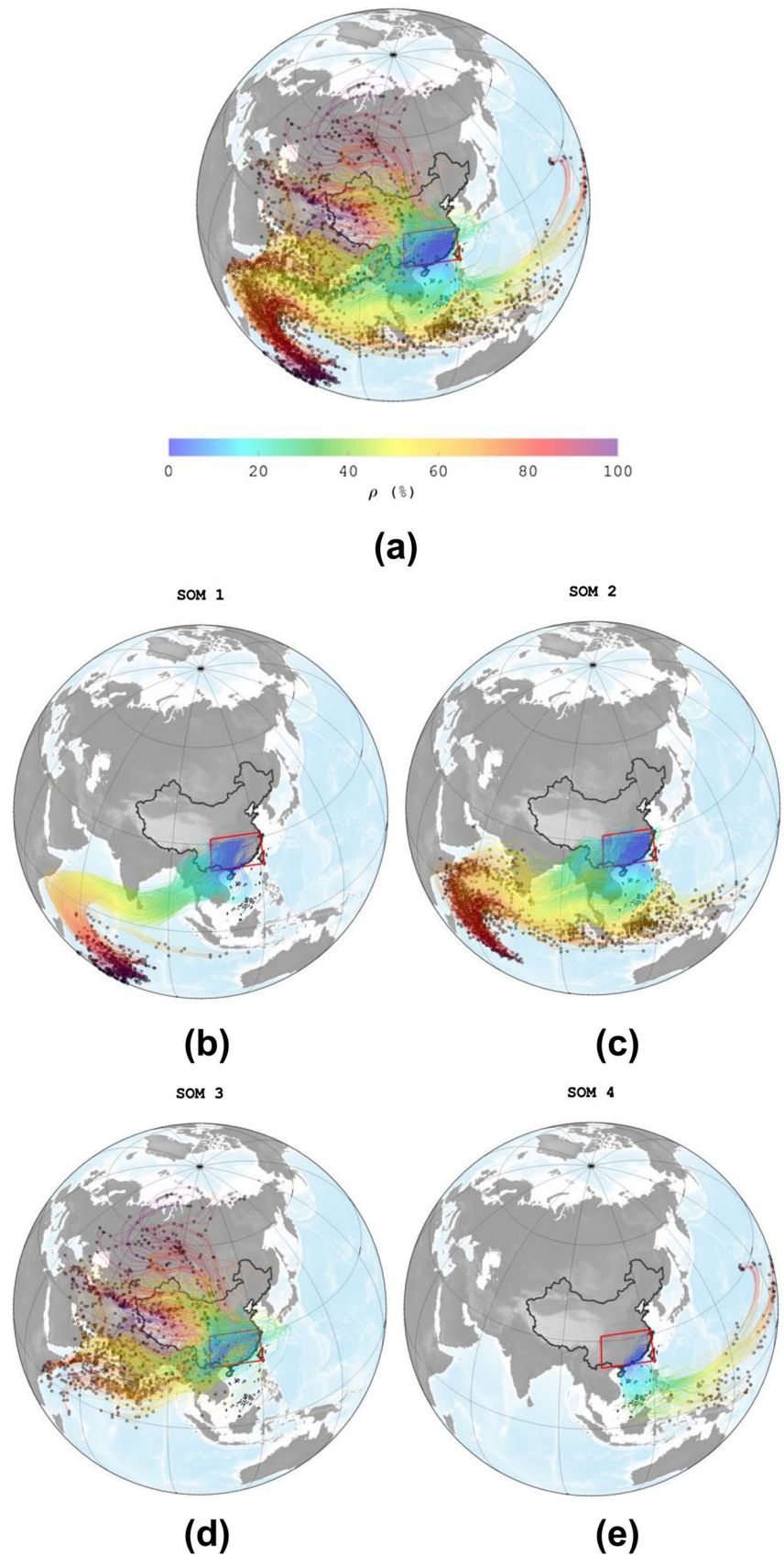
where t denotes the current iteration or time, $\alpha(t)$ the learning rate, $h_{ci}(t)$ is the neighborhood kernel which is commonly a function inversely proportional to the distance and time from the winner unit c at time t. The above iterative procedure tends to project similar patterns of input data onto the neighboring units, thus leads to a topological map of data (Liu et al. 2006b).

For the input data in large size, such as the long-term trajectory data, another training process named batch algorithm is more frequently used. Instead of processing a single data vector at a time, the batch version of training simultaneously updates all the weight vectors through partitioning input data into a set of Voronoi sets by minimum Euclidian distance. The mean of data vectors in each set is

$$\mathbf{V}_i(t) = \frac{1}{n_{V_i}} \sum_{j=1}^{n_{V_i}} \mathbf{x}_j, \tag{3}$$

where $\mathbf{V}_i(t)$ is the Voronoi set of unit i, n_{V_i} the number of samples of the Voronoi set. The batch algorithm then updates the weight vectors by the rule (Liu et al. 2006b):

$$\mathbf{m}_i(t+1) = \frac{\sum_{j=1}^{m} n_{V_j} h_{ij}(t) \mathbf{V}_j(t)}{\sum_{j=1}^{m} n_{V_j} h_{ij}(t)}, \tag{4}$$

where m is the number of map units.

In this study, SOM Toolbox downloaded from http://www.cis.hut.fi/projects/somtoolbox/ is employed to extract the primary moisture transport pathways based on the trajectories data from spatially unbounded DRM mentioned in Sect. 2.2. Here, three properties of trajectories are used to identify different trajectory classes, i.e., the trajectory location ($\mathbf{S} = [S_x, S_y]$), trajectory slope ($\mathbf{U} = [U_x, U_y]$) and concavity ($\mathbf{A} = [A_x, A_y]$), each including two (longitude and latitude) components. Thus, the matrix of input data for SOM has the form of

$$\mathbf{C}_{in} = \begin{pmatrix} \mathbf{S}_{1,1} & \cdots & \mathbf{S}_{1,N} & \mathbf{U}_{1,1} & \cdots & \mathbf{U}_{1,N} & \mathbf{A}_{1,1} & \cdots & \mathbf{A}_{1,N} \\ \vdots & \ddots & \vdots & \vdots & \ddots & \vdots & \vdots & \ddots & \vdots \\ \mathbf{S}_{M,1} & \cdots & \mathbf{S}_{M,N} & \mathbf{U}_{M,1} & \cdots & \mathbf{U}_{M,N} & \mathbf{A}_{M,1} & \cdots & \mathbf{A}_{M,N} \end{pmatrix}, \tag{5}$$

where $\mathbf{C}_{in}$ is the input matrix for the SOM toolbox, M the number of the trajectories, N the number of the time levels of each trajectory. Through the SOM training procedure, we will extract the topological map represented by the BMUs with taking the above three properties of trajectory into account. In this study, there are totally 135 grid cells in SC. For the 37 summers during 1979–2015, the total number of trajectories is $M = 459{,}540$, i.e., 135 grid cells × 92 days/summer × 37 summers. The 15-day trajectory in 6-h sampling has 61 temporal levels ($N = 61$). Thus, the column number of $\mathbf{C}_{in}$ is 3 properties × 2 components × 61-time

levels, i.e., 366. For the input matrix in such a large size of $459{,}540 \times 366$, the batch training algorithm is chosen due to its higher efficiency compared to the sequential one (Liu et al. 2006b).

Figure 2 demonstrates an example of the SOM clustering for the spatially unbounded DRM-produced moisture trajectories in a typical summer month. We can roughly discern the principal moisture pathways to SC from the overall moisture trajectories shown in Fig. 2a, including the pathways from upstream Eurasia, the Indian Ocean, South China Sea, and the Western Pacific. Figure 2b–e are the four clusters through projecting the overall trajectories in Fig. 2a onto a 2 × 2 map by the SOM training procedure. The original input moisture trajectories are therefore classified into four units, each representing a climate mode of the moisture pathway. From Fig. 2b–d, the four units reflect the moisture transports by cross-equatorial flow from the Somali area (SOM1), southwest/south flows from the Arabian Sea, the Bay of Bengal and the South China Sea (SOM2), two branches of westerlies around Tibet Plateau (SOM3), and the southeast flow from Western Pacific (SOM4). This result reflects the influence of the main circulation systems dominating the summer rainfall in SC. Although Fig. 2 shows the clusters based on only one-month data, the extracted characteristics are highly consistent with those from 37-summer clustering shown in Fig. 5, suggesting that the topological structure of the moisture transport of SC is robust in the study period.

For the overall 37-summer data, we implement the SOM control run by using a 2 × 2 rectangular-lattice map. Several other runs in larger maps, such as 2 × 3 and 2 × 4 maps are also implemented to test the clustering sensitivity. Although more nodes/classes can isolate more classes of moisture pathways and thus show more detailed characteristics of moisture transport, all the sensitive runs reach the qualitatively similar features of transport classes like the 2 × 2 map.

That is to say, four nodes (2 × 2) is enough to describe the primary pathways of moisture transport to the SC precipitation in summer.

2.4 Projection time series of trend and estimation of trend contribution

In order to investigate the atmospheric circulations associated with the precipitation trend, we project the precipitation onto its linear trend at the monthly timescale by the approach of projection time series, which can be used to measure how

closely the variable resembles its trend pattern (Feldstein 2002; Park et al. 2015). The projection time series (P_t) is given by

$$P_t = \sum_{i=1}^{N} x_i \dot{x}_i \cos^{1/2} \theta_i, \tag{6}$$

where N is the number of grid points in the study region, x_i and $\dot{x}_i$, respectively, are the normalized precipitation percentage anomaly itself and its linear trend at the grid cell i with area weighting for the variance by the square root of the cosine function of latitude (θ_i). Moreover, the monthly projection time series of the moisture contribution for each SOM class is constructed. Before regressing the atmospheric variables against P_t, interannual variability has been removed by subtracting the summer mean for each year because the sub-annual, particularly, the intra-seasonal atmospheric variability mainly manifests itself as the large-scale teleconnections with stronger modulation on the variability of midlatitude weather than inter-annual and longer variabilities (Hoskins et al. 1983; Luo 2005; Luo et al. 2011). Previous researches (Park et al. 2015; Goss et al. 2016) extracted the large-scale circulation patterns associated with the long-term trends of sea ice and the Arctic warming by compositing the sub-annual circulation fields against the trend P_t by removing the seasonal means or filtering out the variabilities longer than inter-annual timescale. In our study, the linear resonance between the circulation and the precipitation trends also concentrates at intraseasonal timescale (figures not shown). Hence, removing the summer means from the correlation analysis is conducive to extract typical circulation pattern associated with the long-term precipitation trends, which are mainly contributed by the events at intraseasonal timescale. It is noteworthy that the correlation analysis carried out in the following content has considered the effective degree of freedom by the method presented by Quenouille (1952) to take into account the reduction of the degree of freedom by the auto-regressive characteristics.

For the precipitation in the target region, this study also quantitatively estimates the trend contributions from different moisture transport pathways with referencing to the method by Park et al. (2015), which is a simple linear method commonly used to estimate the relative importance between several contributors to a trend. In the linear frame, for the precipitation (P) in the target region, the ratio of precipitation trend (ΔP) explained by the moisture contribution (P_m) from a specific pathway is calculated by $(b_{P,P_m} \Delta P_m)/\Delta P$, where b_{P,P_m} is the regression coefficient between the detrended P and detrended P_m, and ΔP_m is the linear trend of P_m. This method assumes the ratio between the trend contribution from P_m and its trend (ΔP_m) is determined by the linear relationship between the detrended time series of P and P_m. That is a simplified linear method without considering the nonlinear relationship between the target trend and the contributors. However, it is still meaningful to show the relative contribution between difference trend sources in the linear regime. As mentioned in Sect. 2.2, the extended DRM can impossibly trace 100% of the moisture contribution evaporating from the entire globe. The moisture contribution of the undetected moisture sources is excluded from the analysis. Thus, instead of discussing the absolute contribution from the incomplete sources, we focus on the relative one to find the moisture transport pathways linearly contributing to the precipitation trend in the target region.

3 Results

3.1 The interdecadal trend transition of precipitation

Summer precipitation of East China has undergone abrupt changes in the end-1970s (Ding et al. 2008) and mid-1990s (Si and Ding 2013). As a part of East China, SC mainly explains the precipitation regime shift in the 1990s. Figure 1b displays the variation of anomalous precipitation percentage (referred to as precipitation hereafter) in summer months in SC during 1979–2015. At first glance of Fig. 1b, the regional precipitation of SC displays an interdecadal undulation peaked in about the year 1997. This interdecadal precipitation variation spans the period of 1983–2013, which is composed of a significant upward trend during 1983–1997 (T1) and a significant downward trend during 1998–2013 (T2). To some extent, the trend transition between T1 and T2 can be approximately explained a quasi-30-year oscillation. The mean SC precipitation from ERAI reanalysis highly correlates with that from GPCC ($r = 0.9$ at $p < 0.05$) and station observation ($r = 0.77$ at $p < 0.05$). When it comes to the projection time series of the SC precipitation trends (Fig. 4a), the three data also show consistent trend changes although the ERAI reanalysis overestimates the trend magnitude. The Mann–Kendall trend tests show that both the increasing and decreasing trends of precipitation exceed 95% confidence level for all the three datasets used here. Furthermore, the spatial distributions of the precipitation trends identified from ERAI and the other two datasets coincide well (figure not shown). That further confirms the robustness of the existence of the trend transition. The transition point between the two precipitation trends is generally as that in previous work (Ding et al. 2008; Si and Ding 2013).

The spatially unbounded DRM is used to quantitatively estimate the moisture contribution of the water vapor sources for the SC precipitation. Figure 3a shows the long-term mean moisture sources and their contributions to the SC summer rainfall based on the 15-day Lagrangian backward

Fig. 3 The temporal means and variations of the moisture contributions to the summer precipitation of SC: **a** spatial distribution of the climatological mean moisture contribution (mm day⁻¹) to the summer precipitation in SC (black box) during 1979–2015. **b** The time series of local (solid green line) and external (solid red line) moisture contributions (mm day⁻¹). The thick straight lines are the linear trends during the two sub-periods (1983–1997, T1 and 1998–2013, T2). The linear trend slopes (mm day⁻¹ decadal⁻¹) of the two sub-periods are shown in the bottom part of the plot, where the symbol * and **, respectively, represent the Mann–Kendall test at the significance level of $p < 0.10$ and $p < 0.05$
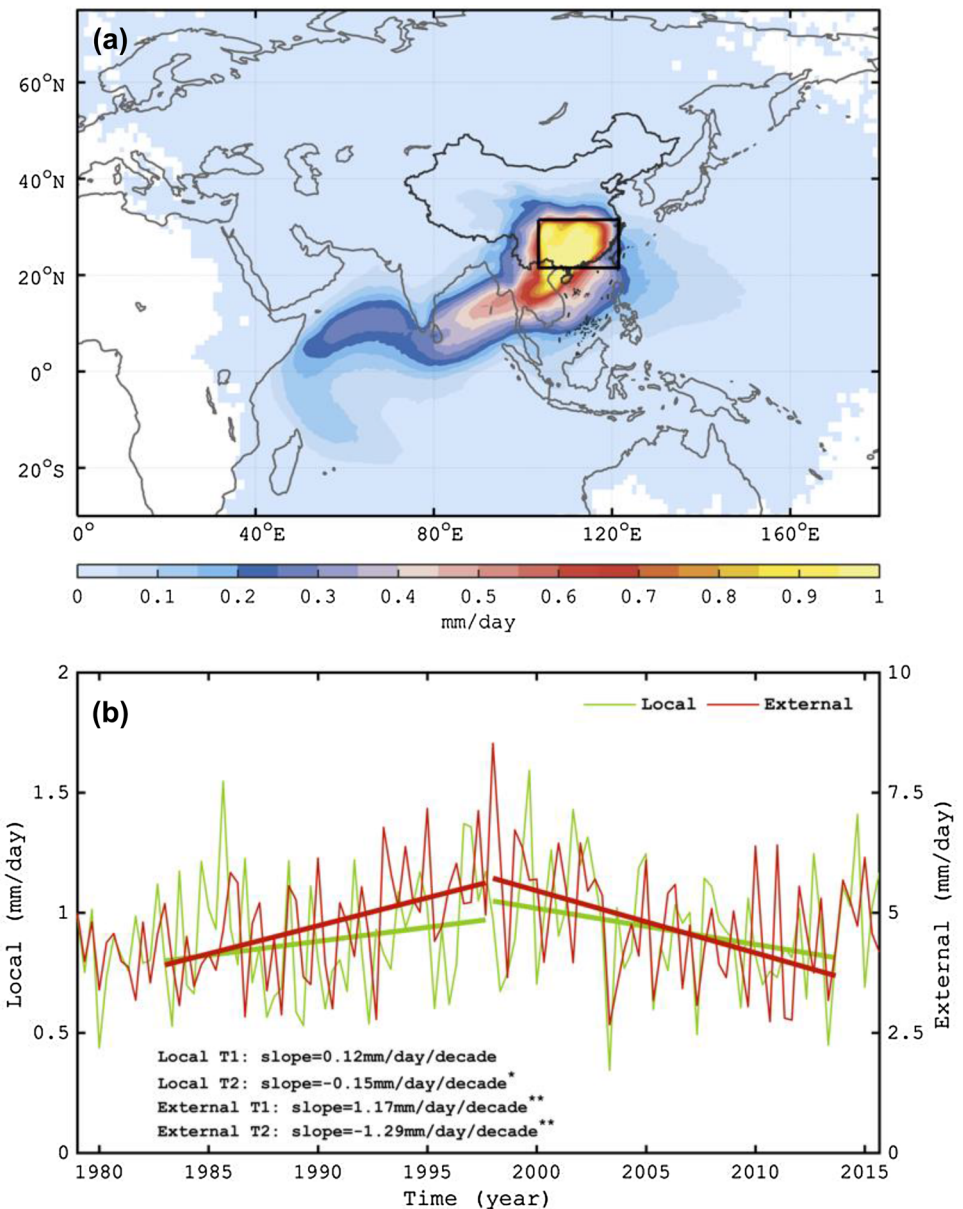
moisture tracing. The spatial extent of the sources covers the Eurasia continent, the Arctic, the Western Pacific, and the north and the tropical Indian Ocean. The main moisture sources that dominate the SC rainfall are located in SC itself, the Arabian Sea, the Bay of Bengal, Southeast Asia, and the South China Sea. Those source regions are generally consistent with previous studies (Chen et al. 2013; Drumond et al. 2011; Wei et al. 2012). As the high-valued area shown in Fig. 3a, short-distance moisture contribution including that from SC itself and Southeast Asia provides a substantial amount of water vapor. Although the external sources show dispersed distribution, the climatology of moisture contribution still shows the principal pathway of long-distance moisture transport from the east coast of Africa via the tropical western Indian Ocean, the Arabian Sea, the Bay of Bengal

and finally through Southeast Asia to SC. This long-distance transport belt is highly modulated by the cross-equatorial flow around the Somali area, which has been found to have a strong influence on the precipitation of Yangtze River Basin, a north part of SC (Fan 2006; Chen et al. 2013).

To understand the physical processes causing the interdecadal transition of precipitation trends shown in Fig. 1b, it is a better way to separate the local recycling process from the external one. The spatially unbounded DRM provides us with such a powerful tool to identify the local contribution and the external contribution for the target precipitation (Hua et al. 2017b). The time series in Fig. 3b separately illustrate the temporal variations of the moisture contributions due to the local and external moisture sources. As shown in Fig. 3b, the external moisture contribution is about
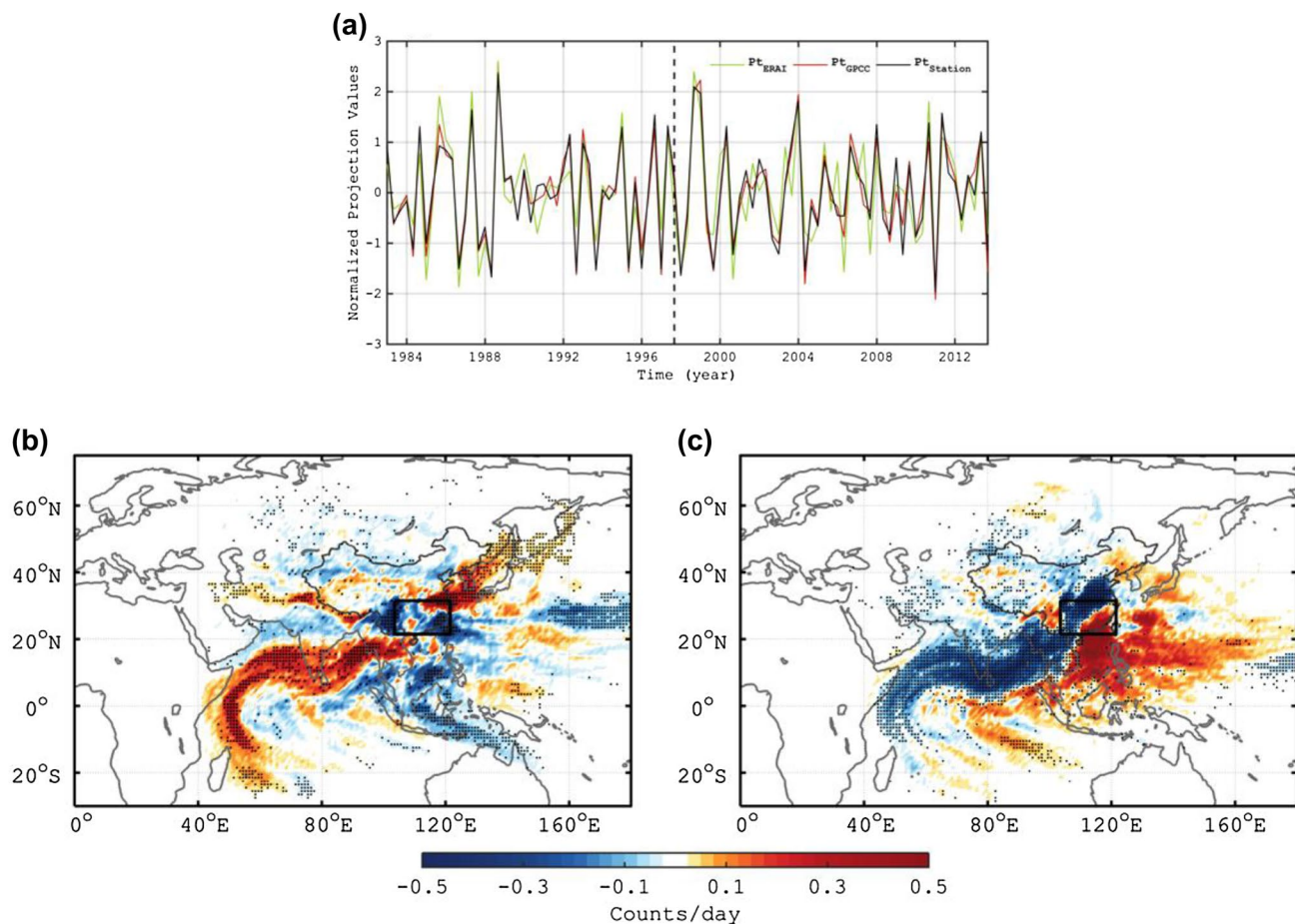
Fig. 4 The monthly projection time series (P_t) of the precipitation trend and the linear regression of the moisture trajectory counts on P_t: **a** the P_t time series projected on the precipitation trends extracted from different precipitation datasets in T1 and T2, where the P_t series is constructed separately for T1 and T2 but then concatenated as one; **b**, **c** the linearly regressed trajectory count against P_t for the period for T1 (**b**) and T2 (**c**). The thick vertical line in **a** marked the precipitation trend transition year (1997). The stippled area in **b** and **c** indicates the regressions at the significance level of $p < 0.05$

five times the magnitude of the local contribution. On average, the regional moisture recycling ratio, i.e., the moisture contribution of the locally evaporated water to the precipitating water in the same region (Burde and Zangvil 2001), is about 16% during the summer months studied here. In other words, 84% of the SC summer precipitation is supported by the external moisture sources. Chen et al. (2013) used a Lagrangian method to quantify the relative contribution to the precipitation in the Yangtze River Basin (YRB) that partly overlaps SC. They concluded that about 78% of YRB rainfall is contributed by the sources over the North Indian Ocean and the Western Pacific. For SC, Li et al. (2012) found the 91% of total net moisture inflow is from western and southern boundary of SC, suggesting the role of westerlies and southwest flow. However, all the previous did not directly estimate the ratio between local and external sources. It should be noted that the regional recycling ratios partly depend on the region's size and its shape (van der Ent

et al. 2010). The regional recycling ratio of an extremely small region is about 0, but going to 1 for a region encompassing the global area. Previous researchers have found that there exists a nonlinear relationship between recycling ratio and the region's area (Dirmeyer and Brubaker 1999; Hua et al. 2017a), in which the increasing rate of regional recycling ratio slows down with region's area, particularly when the area exceeds a threshold value. In China, the threshold area is about 1×10^6 km^2 (Hua et al. 2017a), which is much smaller than the area of SC, $\sim 1.7 \times 10^6$ km^2. That confirms the dominant role of the external sources in the moisture contributions to the SC rainfall even if we change the spatial scale of SC within a substantial range.

Figure 3b presents the linear trends of the local and external moisture contribution. During the subperiods 1983–1997 and 1997–2013 (T1 and T2 in Fig. 1b), the interdecadal trends displayed in the local contribution are not as remarkable as the external part. The local moisture contribution

has no significant trend in T1 and a weak trend in T2. However, for the external contribution, both of the two sub-periods show significant trends over 95% confidence level, being highly consistent with the interdecadal trend of the SC precipitation shown in Fig. 1. Through using a simple linear method (Park et al. 2015), we further estimate the trend contributions by local and external sources, respectively. Relatively speaking, the local and external sources, respectively, account for about 16.1% and 83.9% of the SC precipitation trend in T1, and 28.9% and 71.1% in T2. The precipitation trend explained by the local moisture is of a relatively smaller fraction, especially in T1. In T2, the ratio of the trend explained by the local moisture has increased nearly threefold, implying the enhancement of the recycling process in the second period. Overall, the moisture sources outside of SC are mainly responsible for the interdecadal variation of the precipitated moisture and thus the precipitation in SC.

In order to examine the relationship between the precipitation interdecadal variation and its moisture transport processes, the monthly projection time series (P_t) (Park et al. 2015) of the precipitation is constructed for the precipitation trends in T1 and T2, respectively. The resulted P_t series (Fig. 4a) reflects the strength that the monthly precipitation contributes to the trends in the two sub-periods. It is noteworthy that the P_t series is constructed separately for T1 and T2 firstly and then combined into one time series in Fig. 4a. The P_t series based on all the three datasets well coincide in T1 and T2 with the ERAI-GPCC and ERAI-Station correlations of 0.8–0.9 at $p < 0.01$. Because the P_t series reflects the contribution of the precipitation variation at monthly scale to the long-term trend, the high consistency between the P_t series from different datasets thereby confirms the robustness of the trends and trend transition, and also the reliability of ERAI for this issue.

Through using the P_t time series, we can further project the associated moisture transport by simple linear regression or correlation. As mentioned by Sect. 2.3, the spatially unbounded DRM used here quantitatively calculate the moisture contribution along the Lagrangian backward moisture trajectory. With the information of the Lagrangian trajectories, we can easily obtain the distribution of the moisture transport pathways through summing up the trajectory number over each grid cell. The moisture trajectory counts provide a reasonable representation of the moisture transport trajectory movement (Alexander et al. 2015). Figure 4b, c show the maps of the linear regression of moisture trajectory counts on the monthly P_t for T1 and T2, respectively. Before applying the regression analysis, we have removed the monthly calendar means from the time series of trajectory count over each grid cell. The regressed count maps generally indicate that a west–east seesaw pattern, in which the positive/negative anomalies indicate increasing/

decreasing pathways of moisture transport to SC. The similar seesaw pattern was also found in the moisture flux to other region of East China, such as YRB (Wei et al. 2012). Here, we further establish the linkage between the interdecadal trend transition and the pattern of moisture transport. For the upward precipitation trend in T1 (Fig. 4b), the positive anomalies concentrate along an enhanced southwest transport pathway originated from the west Indian Ocean and steered eastward through the Arabian Sea and the Bay of Bengal and finally entered SC via Indo-China Peninsula. Thus, more moisture transport through this southwest pathway results in the increasing summer precipitation in SC in T1. When compared to the enhanced southwest transport, the weakened east and southeast transport from the Western Pacific and Southeast Asia is found at the same time. However, for T2 (Fig. 4c), the opposite pattern featured by the weakened southwest transport but enhanced east and southeast transport corresponds to the downward precipitation trend in SC. To a great extent, the competition between southwest transport and east/southeast transport determines the interdecadal variation of the SC summer precipitation during the study period.

3.2 Contribution of the moisture transport pathways to trend transition

With the general image of the water transport (Fig. 4b, c), the SOM clustering is applied to disentangle the water vapor transport pathways and their variations further. As mentioned in Sect. 2.3, the 2 × 2 map (i.e., four nodes) is used to classify the moisture pathway clusters for the Lagrangian moisture trajectories of SC. Figure 5 shows the composite means of the moisture trajectory count for the four SOM classes. One of the prominent features of Fig. 5 is that all except for SOM3 (Fig. 5c) have remarkable external moisture originated from oceanic regions. The mode SOM1 (Fig. 5a) indicates the cross-equatorial transport in the western part of the tropical Indian Ocean (referred to this mode as TIO). Along the TIO transport pathway, high trajectory counts are located in the Somali Basin, the Arabian Sea and the Bay of Bengal. This water vapor transport branch reflects the effect of the Somali cross-equatorial flow (Joseph and Sijikumar 2004). The cross-equatorial flow can transport water vapor through the equator from the southern hemisphere to the northern hemisphere and then influence the East Asian summer rainfall (Wang and Xue 2003). Figure 5b (SOM2) displays relatively shorter pathway mainly from the Arabian Sea and the Bay of Bengal, which covers the northern Indian Ocean, the South China Sea and the Maritime Continent (referred to as ISM hereafter). This robust southerly water vapor transport from the South China Sea and the Maritime Continent primarily dominates this pattern. The trajectory distribution of mode SOM3 (Fig. 5c) suggests the
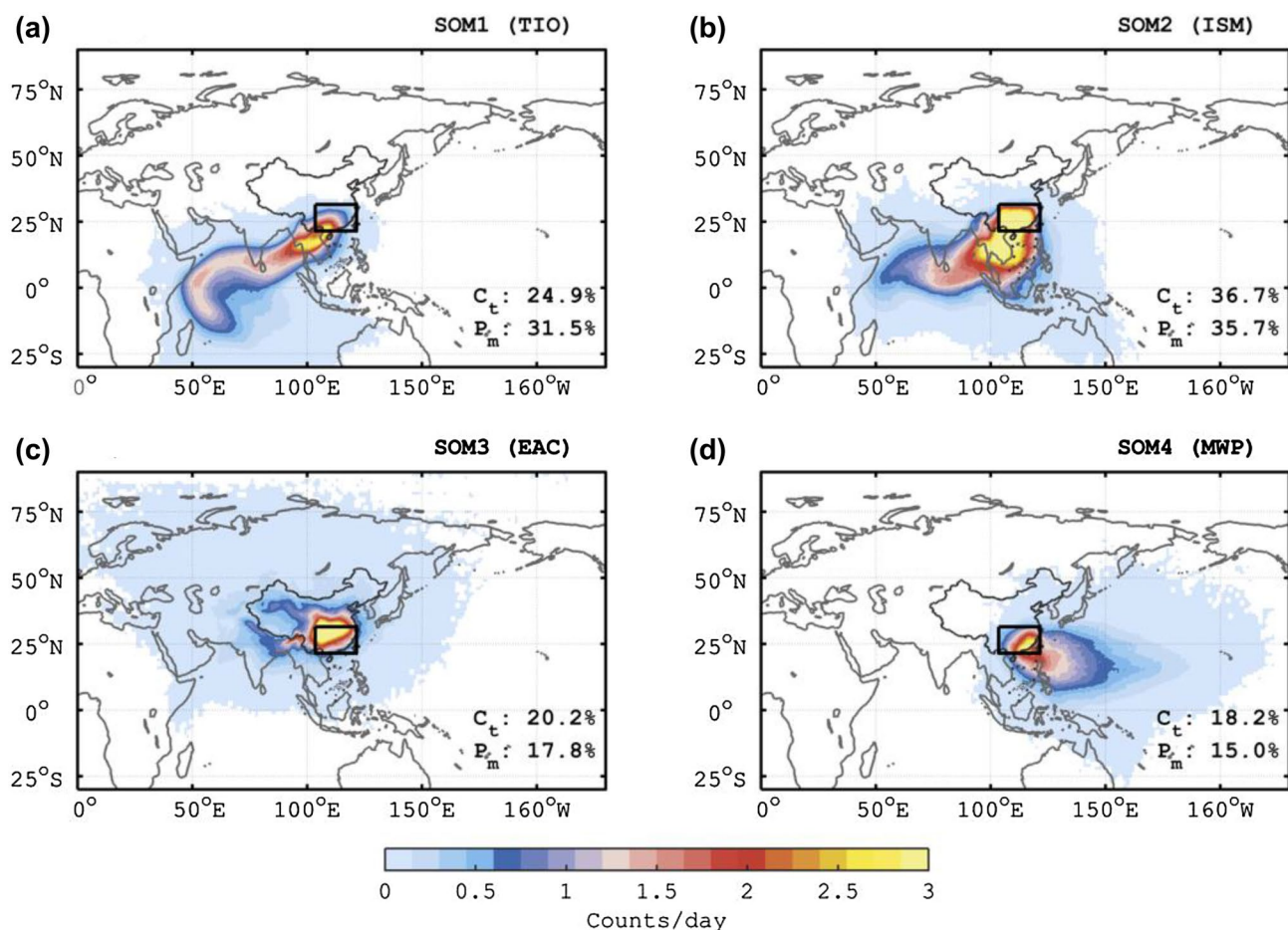
Fig. 5 Composite means of the moisture trajectory count for SOM clusters: **a** SOM1 (TIO), **b** SOM2 (ISM), **c** SOM3(EAC) and **d** SOM4 (MWP). The black box in each plot marks the region of SC. The percentages shown in the bottom right corner of each panel are the fractions of the trajectory count contribution (C_t) and precipitation contribution (P_m) explained by the corresponding SOM mode during 1983–2013

contribution due to the terrestrial moisture sources located in almost the whole Eurasia continent (referred to EAC hereafter). The evaporative water vapor in EAC is transported along relatively more dispersed routes and intrudes SC mainly through west and north boundaries of Tibet Plateau. The westerly water vapor transport originated from Eurasia continent and even the Atlantic Ocean and the Arctic Ocean mainly dominate mode EAC. For SOM4 (Fig. 5d), the trajectory concentrates over the Western Pacific and the marginal seas south and east to China (referred to as MWP hereafter).

To a great extent, the four SOMs mainly reflect the influences of South Asia Monsoon, South China Sea monsoon, westerly and East Asia monsoon. As shown by the percentages in each plot of Fig. 5, the first two SOMs (TIO and ISM) carry more than 67% (31.5%+35.7%) moisture to SC. This high ratio suggests the primary sources for the SC precipitation are in the Indian Ocean, the South China Sea and the maritime continent in Southeast Asia. And the moisture

contribution from Eurasia (SOM3) (17.8%) and the Western Pacific (SOM4) (15%) only explains a small fraction of the SC precipitation, less than half of the moisture amount conveyed by SOM1 and SOM2, which quantitatively confirms that the tropical Western Pacific only plays a minor role in the water vapor contributors to the SC precipitation (Chen et al. 2013).

As mentioned in Sect. 3.1, the external sources mainly explain the precipitation trend in SC in both T1 and T2. Here, the SOM clusters provide us a way to disentangle the contributions from different sources to the precipitation trend. Table 1 presents the relative trend contribution from each SOM to the trend of the SC precipitation in the two sub-periods. At first glance of Table 1, the MWP pathway (SOM4) has almost no contribution (3.0% and 1.4%) to the precipitation trends in T1 and T2. For the upward trend in T1, mode TIO (SOM1) explains about one-half (50.4%) of the precipitation trend, exceeding the sum of the contribution from the rest three SOM modes. In T2, mode ISM (SOM2)

Table 1 The ratios of the precipitation trend explained by the primary moisture transport pathways

	TIO (SOM1) (%)	ISM (SOM2) (%)	EAC (SOM3) (%)	MWP (SOM4) (%)
T1	50.4	26.3	20.3	3.0
T2	15.2	51.2	32.2	1.4

The percentages (%) in the table represent the explained ratio of the SC precipitation trends by the four SOMs in T1 and T2

is the largest contributor, also explaining more than one-half (51.2%) trend. The mode EAC (SOM3) as the third (20.3%) and second (32.2%) contributor in T1 and T2, respectively, emphasize the important role of the variation of the westerly transport. It can be concluded that the enhancing water vapor transport from the west (SOM3) and the north Indian Ocean (SOM1,2) mainly results in the upward trend of the SC precipitation in T1, but the weakening westerly transport from Eurasia (SOM3) and short-distance southwesterly transport from the east Indian Ocean (SOM2) dominates the decreasing precipitation trend in T2. Above features can also be discerned in the pathway trend shown in Fig. 4 except that Table 1 presents quantitative estimations for different types of transport pathways.

3.3 Large-scale circulation associated with precipitation trend shift

3.3.1 Circulation patterns contributing to precipitation trends

Based on the projection time series (P_t) in Fig. 4a, the correlation maps between P_t and circulation field at 500 hPa are calculated to show the circulation patterns dominate the precipitation trend in T1 and T2, respectively. Figure 6 shows the correlation results from ERAI, GPCC and Station observation. For the P_t series from different datasets, the responses of the circulation field show highly consistent patterns both in T1 and T2, which again confirms the consistency of the precipitation trend between the three datasets. In T1 (Fig. 6a, c, e), the circulation pattern associated with the upward precipitation trend is characterized by a wide belt of strong positive anomalies in the tropic, a zonal wave-train structure in midlatitudes, and quasi-meridional wave-train structure along the west boundary of Western Pacific. The zonal wave train has the positive and negative anomalies spanning Eurasia with its origin located in North Atlantic, where there exists a tilted North Atlantic Oscillation-like structure (Barnston and Livezey 1987; Luo and Gong 2006; Luo et al. 2014, 2018). The index of this zonal wave train (see below) shows significant correlation (r = −0.23 at p < 0.05) with the circumglobal teleconnection

(CGT) related to the variability of the westerly jet stream (Ding and Wang 2005). To the east of the zonal wave train, the anomaly centers arranging along the western boundary of Pacific shows a tilting meridional structure (index see below) like the PJ pattern (Yu et al. 2012; Chen and Zhou 2014), with the correlation of r = −0.32 at p < 0.01. The coupling between the south edge of the zonal wave train and the anti-cyclonic anomaly located in tropic tends to drive the moisture over North Indian Ocean moving eastward and finally steer northward into SC.

With compared to T1, T2 (Fig. 6b, d, f) has the much weaker zonal wave train but the enhanced opposite PJ-like meridional wave train. The positive tropical anomalies also disappear. This kind of pattern tends to reinforce the short-range moisture transport from the South China Sea and Western Pacific, but inhibit the long-range transport from the Indian Ocean and the upstream area in Eurasia. Almost individually controlled by the quasi-meridional wave train, the moisture contribution from the main source regions dramatically reduces, and thus the downward rainfall trend occurs in T2.

3.3.2 Coupling between wave-train structures

It seems that the coupling of the above-mentioned two wave trains is a crucial factor in determining the location of the moisture source. To further explore the role of wave trains, we define the monthly zonal wave train index (WT_z) as the normalized height difference between the Z500 in box 3 and box 4 in Fig. 6a, i.e., $WT_z = \mathbf{Z}(Z500_3 − Z500_4)$, where $\mathbf{Z}$ is normalization operator, $Z500_n$ ($n = 3, 4$) is the spatial mean of Z500 in No. n box in Fig. 6a. In the same manner, the quasi-meridional wave train index is defined as $WT_m = \mathbf{Z}(Z500_1 − Z500_2)$. With the two wave-train indices, we further study the distribution of the precipitation events in WT_z–WT_m plane in Fig. 7, in which the red/blue circle represents the positive/negative precipitation event. Here, the precipitation event is defined based on the monthly P_t, in which a positive/negative P_t month corresponds to a positive/negative precipitation event contributing to the precipitation trend. The linear-fit slope of the precipitation events in WT_z–WT_m plane reflects the coupling strength between the zonal and meridional wave trains, i.e., more significant slope suggesting a higher probability of the concurrence of the two wave trains.

Figure 7a displays the distribution of the precipitation events in T1. The positive events are mostly in the first quadrant of Fig. 7a, but negative events in the third quadrant, showing a significant slope of $b = 0.45$ over the 99% significance level. Correlation analysis also shows significant positive WT_z–P_t and WT_m–P_t correlations for the three precipitation datasets. That suggests the coupling between positive-phase zonal wave train (WT_z+) and positive-phase
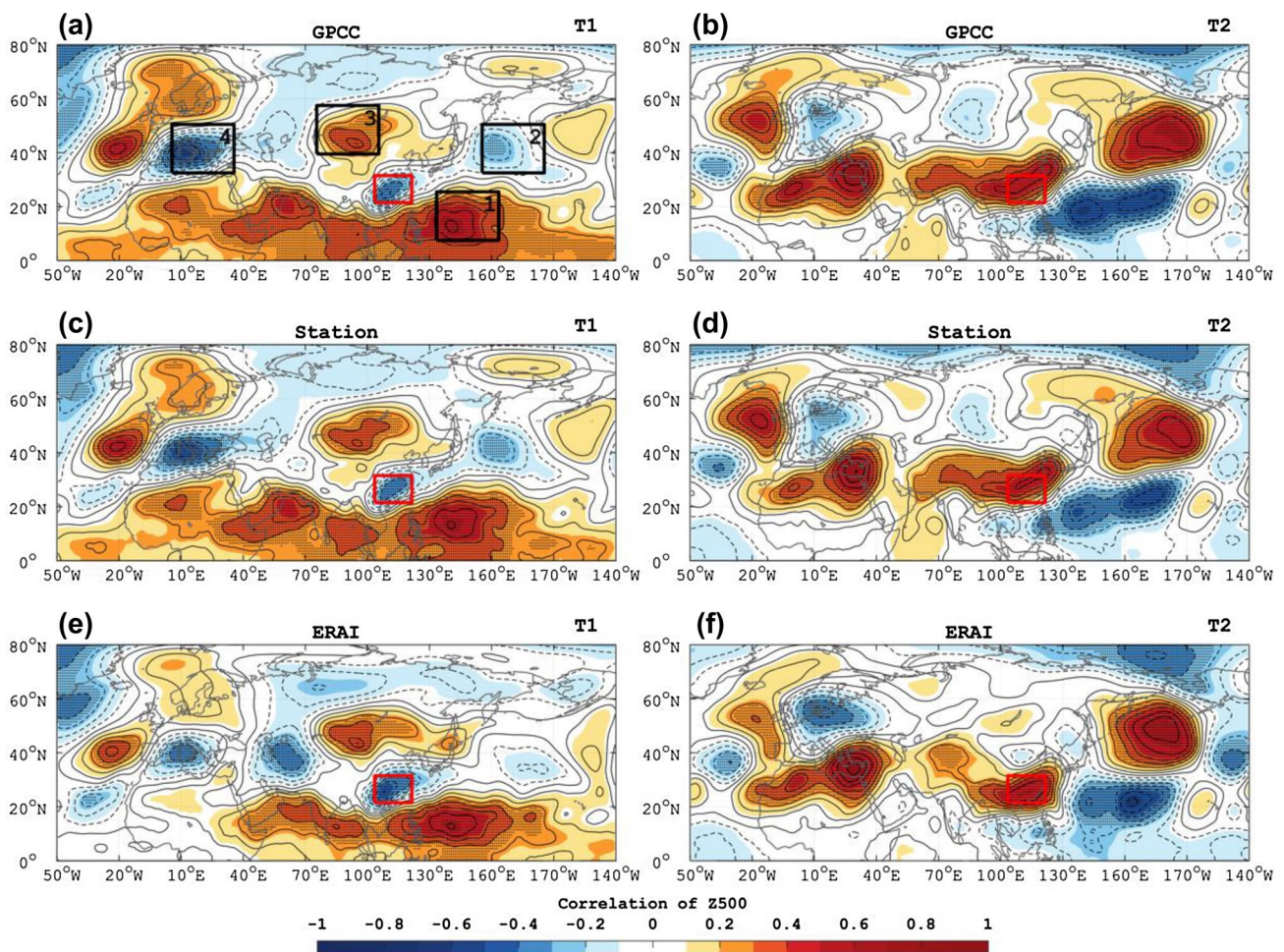
Fig. 6 Correlation map between projection time series (P_t) of precipitation trend and the anomalous geopotential height at 500 hPa (Z500): **a**, **c** and **e** for the upward precipitation trend in T1 based on ERAI, GPCC and station observation, respectively; **b**, **d** and **f** the same but for downward precipitation trend in T2. The red box in each plot marks the region of SC. The black boxes define the spatial ranges used in the construction of the zonal and meridional wave train index, refer to the text for more details

meridional wave train (WT_m+) is a circulation condition significantly enhancing southwest transport flux from the Indian ocean and thus the upward precipitation trend in T1. However, for the downward trend in T2, there is no significant coupling ($b = 0.23$) found between the two wave trains. All the three precipitation datasets show significant negative WT_m–P_t correlations but weak WT_z–P_t correlations for the downward precipitation in T2. It means that the negative-phase meridional wave train individually determines the downward precipitation trend in T2.

Based on the SOM clusters, the circulation associated with moisture contribution of SOM mode can further reveal the circulation components contributing to the total circulation pattern causing the precipitation trend. Figure 8b–i display the correlation maps between the P_t of moisture contribution trend (Fig. 8a) and the circulation field. For the upward trend of moisture contribution in T1 (Fig. 8b, d, f, h), the coupling between zonal and meridional wave

trains can be observed when combing the circulations of the SOM modes although different SOM mode emphasizes different parts of the wave trains. The circulation pattern of TIO mode (SOM1) (Fig. 8b) emphasize the zonal wave train and the tropical anomaly of the meridional wave train, which tends to enhance the long-range moisture transport along the north Indian Ocean. The ISM mode (Fig. 8d) shows strong positive-phase meridional wave train but weak zonal wave train. Thus, this pattern tends to enhance moisture transport from the Bay of Bengal and the South China Sea. Moreover, the circulation of EAC mode (SOM3) (Fig. 8f) is featured by the south shift zonal wave train because this mode is mainly responsible for the westerly moisture transport. As is expected, the MWP mode (SOM4) (Fig. 8h) thus only has prominent anomalous circulation over the Western Pacific. Similarly, for the downward trend in T2 (Fig. 8c, e, g, i), the contributions to the negative-phase of meridional wave train can also be found in SOM1–3 with the well-organized zonal
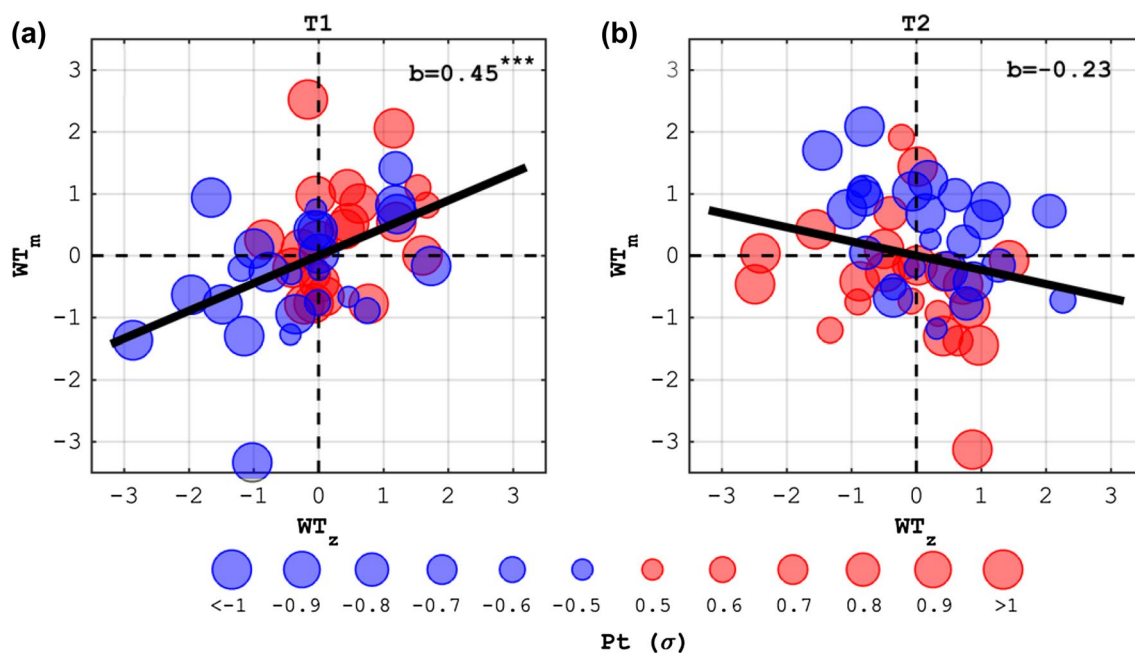
Fig. 7 The distribution of the precipitation events in the WT_z–WT_m plane, where the WT_z and WT_m are the zonal and meridional wave train index, respectively. The detailed definitions of the circulation index WT_z and WT_m can be found in Sect. 3.3. The plots, **a** and **b**, are the distributions of precipitation events in T1 and T2, respectively. The red/blue filled circle in each plot represents the positive/negative precipitation event. The positive/negative precipitation event is the month positively/negatively contributing to upward/downward pre-cipitation trend in T1/T2. Moreover, the size of the circle corresponds to the magnitude of the normalized projection time series (P_t) of the GPCC precipitation trend scaled by the standard deviation (σ) in T1 and T2, just as shown by the legend at the bottom of the figure. The thick black line is the linear fit line of precipitation events with the regression coefficient shown in the upper right corner of the plot. The three asterisks in superscript of the coefficient suggest the regression passing p = 0.01 significance test

4 Discussion and conclusions

This study investigates the interdecadal variability of the summer precipitation in South China (SC) during 1983–2013. It indicates that the summer precipitation over SC has experienced an interdecadal shift in the late 1990s. Multiple observational data and the reanalysis data confirm that a significant increasing trend of the summer rainfall before the year of 1997 (T1) and a significant reverse trend since then (T2). In order to investigate the interdecadal transition of the precipitation trends, the spatially unbounded DRM method is used to identify moisture sources affecting the precipitation and its variation in SC. During the summer season, the primary moisture sources for SC rainfall cover Eurasia continent, the Northern Indian Ocean, and the Western Pacific. The pathways of the moisture transport to SC mainly distribute in the western tropical Indian Ocean, the Arabian Sea, the Bay of Bengal, Southeast Asia, and the

wave train almost absent from the circulation pattern. In particular, the TIO mode has the most distinguished meridional wave train. At the same time, SOM2–3 show relatively weaker and eastward shifting meridional wave trains.

South China Sea. This pattern shows an apparent competition of moisture transport originating between the Indian Ocean and the Pacific Ocean.

On average, about 84% of water vapor for the SC precipitation is from the external moisture sources. So, rather than the water vapor from the local recycling process, the advective moisture is more important for the mean summer rainfall in SC. Moreover, for the interdecadal precipitation variation, the externally sourced precipitation also mainly explains the precipitation trend transition between T1 and T2. In order to explore the precipitation trend-related variation of moisture transport pathway, the distribution of the moisture trajectories of SC is further projected onto the SC precipitation trend in T1 and T2, respectively. Generally, the trend-related distribution pathway shows a seesaw between southwest transport pathway over the Indian Ocean and south/southeast pathway over the South China Sea, Maritime Continent and the Western Pacific.

The method of self-organizing map (SOM) is used to further reveals the primary moisture transport pathways of the SC rainfall. Four pathways are isolated: (1) TIO, the cross-equatorial moisture transport originating from the Somali Basin and through the Arabian Sea and the Bay of Bengal into SC; (2) ISM, the pathway over the Arabian Sea, the
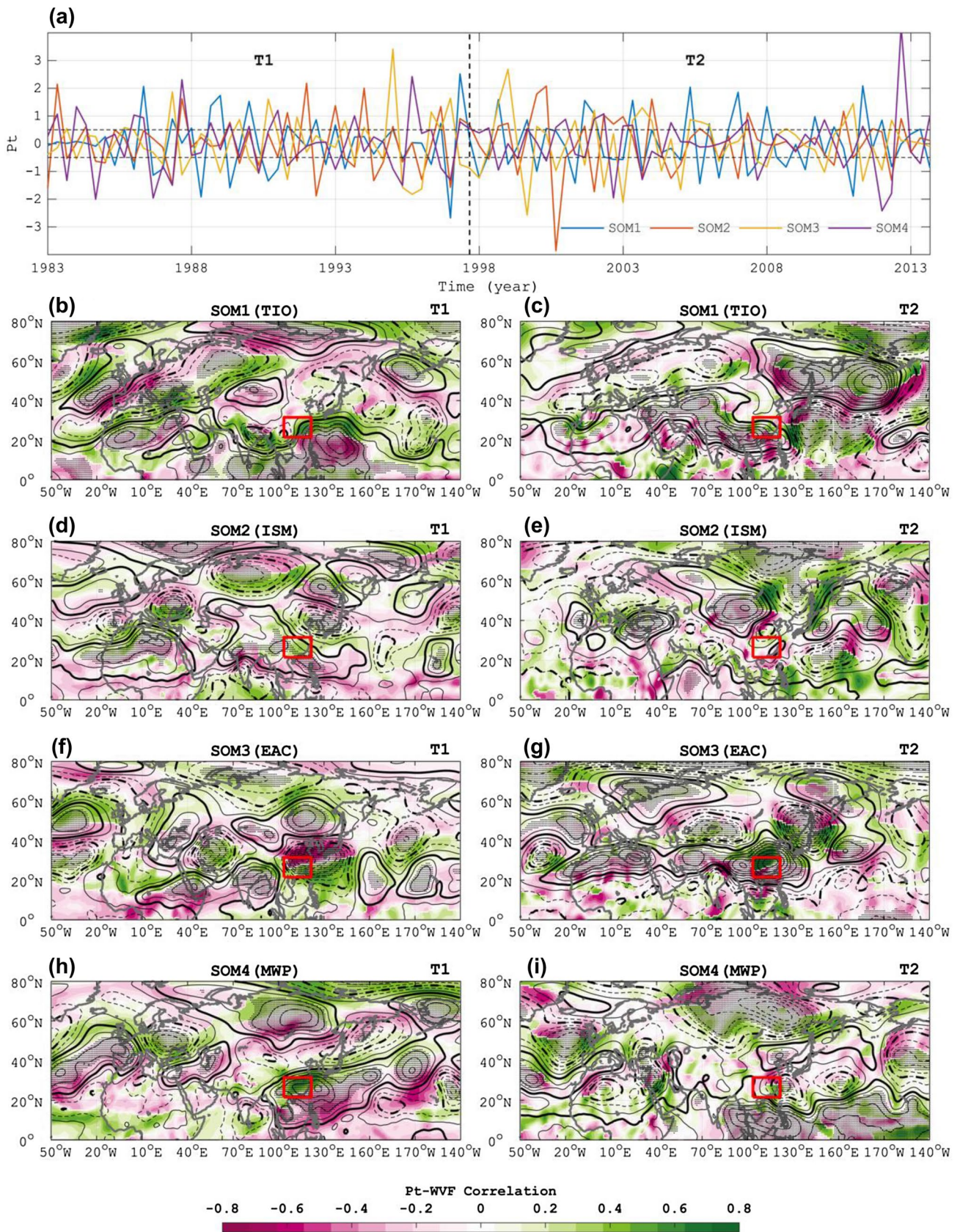
Pt-WVF Correlation

◄**Fig. 8** Correlation maps for SOM mode between the projection time series (P_t) of the moisture contribution trend and the circulation fields: **a** the projection time series (P_t) of moisture contribution trends of the four SOM modes; **b**, **d**, **f** and **h** are, respectively, the correlation maps of the SOM1–4 for the upward moisture contribution trends in T1; **c**, **e**, **g** and **i** are those for the downward moisture contribution trends in T2. The contour is the correlation coefficient between P_t and anomalous 500-hPa geopotential height (Z500) with dashed for negative correlation and bolded for r = ± 0.12. The contour interval is 0.08. The stippled is the correlation over 95% confidence level. The shaded is the correlation between P_t and WVF with green for eastward WVF and purple for westward one

Bay of Bengal, the South China Sea, and Southeast Asia; (3) EAC, the westerly transport pathway over Eurasia terrestrial area with branches at the north and south boundary of Tibet Plateau; (4) MWP, the transport mainly from marginal seas and the Western Pacific. The moisture carried by the two southwest pathway modes (i.e., TIO and ISM), entirely explain the 67% (31.5% + 35.7%) of the SC precipitation, which suggests the water vapor transported by the South Asia monsoon mainly support the water vapor supply of SC. However, the moisture contributed by the westerly (EAC) and East Asia monsoon (MWP) only explains 17.8% and 15% of the SC rainfall, respectively. The dominant roles of the southwest pathways (TIO and ISM) are also prominent in the contribution to the interdecadal variation of the SC precipitation. Quantitative analysis displays that TIO is the most significant contributor to the increasing trend in T1 (50.4%) but ISM is the greatest one to the decreasing trend in T2 (51.2%).

In our analysis, the contribution of Western Pacific (MWP) to the interdecadal variation can be ignored. The moisture transport through pathway MWP is related to the shift of western Pacific subtropical anticyclone (Hsu and Lin 2007). Just as the previous study indicated, the change of the East Asia precipitation in the mid-1990s is uncorrelated to the extension of the western boundary of the western Pacific subtropical high (Kwon et al. 2007). Therefore, it suggests that the interdecadal transition of the SC rainfall in the 1990s is more likely related to the variation of other circulation systems.

We also explored the circulation associated with the trend transition of the SC precipitation. It is found that a well-organized quasi-meridional wave train and a concurrent middle-latitude zonal wave train jointly dominate the increasing precipitation in T1. The zonal wave train spanning Eurasia shows a significant correlation to the circumglobal teleconnection (CGT). The meridional wave train located on the western boundary of Pacific shows the relationship with the Pacific Japan teleconnection (PJ). The zonal wave train seems to transport the energy from the Atlantic to East China coupled with the PJ-like wave train to the east of SC. The match relation between zonal wave train and the meridional pattern enhances the transport along the southwest moisture

pathways over the Indian Ocean, which mainly determines the upward trend of the SC precipitation in T1. However, for the downward trend of precipitation in T2, only a weak coupling between the two wave trains is found. It seems that the enhanced PJ-like meridional wave train individually leads to the downward rainfall trend in T2.

It is noteworthy that the well-organized zonal and meridional wave trains that directly influence the interdecadal variability of the SC rainfall seem to have oceanic origins over the North Atlantic, Indian Ocean, and the Western Pacific. The SSTs of those oceans are likely to modulate the variabilities of the wave trains. In order to reveal the extensive mechanisms of the precipitation variability in SC, the linkage between SST variabilities and the wave trains should be established in future work. Furthermore, more effort is needed on the relative contributions of the SST forcing from different oceans to the variabilities of the SC precipitation. Studying those issues can help us to disentangle the competitive or cooperative relationships between different oceans, and thereby the processes governing the atmospheric circulation patterns associated with the rainfall change in SC.

References

Alexander MA, Scott JD, Swales D, Hughes M, Mahoney K, Smith C (2015) Moisture pathway into the U. S. intermountain west associated with heavy winter precipitation events. J Hydrometeorol 16:1184–1206. https://doi.org/10.1175/JHM-D-14-0139.1

Barnston AG, Livezey RE (1987) Classification, seasonality and persistence of low-frequency atmospheric circulation patterns. Mon Weather Rev 115(6):1083–1126

Burde GI, Zangvil A (2001) The estimation of regional precipitation recycling. Part I: review of recycling models. J Clim 14(12):2497–2508

Cavazos T (2000) Using self-organizing maps to investigate extreme climate events: an application to wintertime precipitation in the Balkans. J Clim 13:1718–1732

Cavazos T, Comrie AC, Liverman DM (2002) Intraseasonal variability associated with wet monsoons in Southeast Arizona. J Clim 15(17):2477–2490

Chen X, Zhou T (2014) Relative role of tropical SST forcing in the 1990s periodicity change of the Pacific–Japan pattern interannual variability. J Geophys Res Atmos 119:13043–13066. https://doi.org/10.1002/2014JD022064

Chen B, Xu X, Zhao T (2013) Main moisture sources affecting lower Yangtze River Basin in boreal summers during 2004–2009. Int J Climatol 33:1035–1046. https://doi.org/10.1002/joc.3495

de Vries AJ, Feldstein SB, Riemer M, Tyrlis E, Sprenger M, Baumgart M, Fnais M, Lelieveld J (2016) Dynamics of tropical–extratropical interactions and extreme precipitation events in Saudi Arabia in autumn, winter and spring. Q J R Meteorol Soc 142(697):1862–1880

Dee DP et al (2011) The ERA-Interim reanalysis: configuration and performance of the data assimilation system. Q J R Meteorol Soc 137:553–597. https://doi.org/10.1002/qj.828

Ding Q, Wang B (2005) Circumglobal teleconnection in the northern hemisphere summer. J Clim 18(17):3483–3505

Ding Y, Wang Z, Sun Y (2008) Inter-decadal variation of the summer precipitation in East China and its association with deceasing Asian summer monsoon. Part I: observed evidence. Int J Climatol 28:1139–1161. https://doi.org/10.1002/joc.1615

Ding Y, Sun Y, Wang Z, Zhu Y, Song Y (2009) Inter-decadal variation of the summer precipitation in China and its association with decreasing Asian summer monsoon. Part II: possible causes. Int J Climatol 29:1926–1944. https://doi.org/10.1002/joc.1759

Dirmeyer PA, Brubaker KL (1999) Contrasting evaporative moisture sources during the drought of 1988 and flood of 1993. J Geophys Res 104(D16):19383–19397

Dominguez F, Kumar P, Liang X, Ting M (2006) Impact of atmospheric moisture storage on precipitation recycling. J Clim 19:1513–1530

Dominguez F, Miguez-Macho G, Hu H (2016) WRF with water vapor tracers: a study of moisture sources for the North American monsoon. J Hydrometeorol 17(7):1915–1927

Drumond A, Nieto R, Gimeno L (2011) Sources of moisture for China and their variations during drier and wetter conditions in 2000–2004: a Lagrangian approach. Clim Res 50:215–225. https://doi.org/10.3354/cr01043

Fan K (2006) Atmospheric circulation in southern hemisphere and summer rainfall over Yangtze River Valley. Chin J Geophys 49(3):599–606

Feldstein SB (2002) Fundamental mechanisms of the growth and decay of the PNA teleconnection pattern. Q J R Meteorol Soc 128:775–796. https://doi.org/10.1256/0035900021643683

Gao H, Wang Y, He J (2006) Weakening significance of ENSO as a predictor of summer precipitation in China. Geophys Res Lett 33:L09807. https://doi.org/10.1029/2005GL025511

Gimeno L, Stohl A, Trigo RM, Dominguez F, Yoshimura K, Yu L, Drumond A, Durán-Quesada AM, Nieto R (2012) Oceanic and terrestrial sources of continental precipitation. Rev Geophys 50:RG4003. https://doi.org/10.1029/2012rg000389

Gong D, Ho C (2002) Shift in the summer rainfall over the Yangtze river valley in the late 1970s. Geophys Res Lett 29(10):1436. https://doi.org/10.1029/2001GL014523

Goss M, Feldstein S, Lee S (2016) Stationary wave interference and its relation to tropical convection and arctic warming. J Clim 29(4):1369–1389

Hoskins B, James I, White G (1983) The shape, propagation and mean-flow interaction of large-scale weather systems. J Atmos Sci 40(7):1595–1612

Hsu H, Lin S (2007) Asymmetry of the tripole rainfall pattern during the east Asia summer. J Clim 20:4443–4458. https://doi.org/10.1175/JCLI4246.1

Hu Z (1997) Interdecadal variability of summer climate over east Asia and its association with 500 hPa height and global sea surface temperature. Geophys Res Lett 102(D16):19403–19412

Hu H, Dominguez F (2015) Evaluation of oceanic and terrestrial source of moisture for the North American monsoon using numerical models and precipitation stable isotopes. J Hydrometeorol 16:19–35. https://doi.org/10.1175/JHM-D-14-0073.1

Hua L, Zhong L, Ke Z (2017a) Characteristics of the precipitation recycling ratio and its relationship with regional precipitation in China. Theor Appl Climatol 127:513–531. https://doi.org/10.1007/s00704-015-1645-1

Hua L, Zhong L, Ma Z (2017b) Decadal transition of moisture sources and transport in Northwestern China during summer from 1982 to 2010. J Geophys Res Atmos 122:12522–12540. https://doi.org/10.1002/2017JD027728

Huang R, Zhang Z, Huang G, Ren B (1998) Characteristic of the water vapor transport in East Asian monsoon region and its difference from that in South Asian monsoon region in summer. Chin J Atmos Sci 22:460–469 (in Chinese)

Jiang Z, Jiang S, Shi Y, Liu Z, Li W, Li L (2017) Impact of moisture source variation on decadal-scale changes of precipitation in North China from 1951 to 2010. J Geophys Res Atmos 122:600–613. https://doi.org/10.1002/2016JD025795

Jin D, Hameed SN, Huo L (2016) Recent changes in ENSO teleconnection over the western Pacific impacts the Eastern China precipitation dipole. J Clim 29:7587–7598. https://doi.org/10.1175/JCLI-D-16-0235.1

Joseph PV, Sijikumar S (2004) Intraseasonal variability of the low-level jet stream of the Asian summer monsoon. J Clim 17:1449–1458

Kalnay E et al (1996) The NCEP/NCAR 40-Year Reanalysis Project. Bull Am Meteorol Soc 77(3):437–472

Keys PW, van der Ent RJ, Gordon LJ, Hoff H, Nikoli R, Savenije HHG (2012) Analyzing precipitation sheds to understand the vulnerability of rainfall dependent regions. Biogeosciences 9:733–746. https://doi.org/10.5194/bg-9-733-2012

Knoche HR, Kunstmann H (2013) Tracking atmospheric water pathways by direct evaporation tagging: a case study for West Africa. J Geophys Res Atmos 118:12345–12358. https://doi.org/10.1002/2013JD019976

Kohonen T (1982) Self-organized information of topologically correct features map. Biol Cybern 43:59–69

Kohonen T (1998) The self-organizing map. Neurocomputing 21:1–6

Kwon M, Jhun JG, Wang B, An SI, Kug JS (2005) Decadal change in relationship between east Asian and WNP summer monsoons. Geophys Res Lett 32:L16709. https://doi.org/10.1029/2005GL023026

Kwon M, Jhun JG, Ha KJ (2007) Decadal change in east Asian summer monsoon circulation in the mid-1990s. Geophys Res Lett 34:L21706. https://doi.org/10.1029/2007GL031977

Li Y, Leung LR (2013) Potential impacts of the Arctic on interannual and interdecadal summer precipitation over China. J Clim 26:899–917. https://doi.org/10.1175/JCLI-D-12-00075.1

Li X, Wen Z, Zhou W, Wang D (2012) Atmospheric water vapor transport associated with two decadal rainfall shifts over East China. J Meteorol Soc Jpn 90(5):587–602. https://doi.org/10.2151/jmsj.2012-501

Liu Y, Weisberg RH, He R (2006a) Sea surface temperature patterns on the West Florida Shelf using the Growing Hierarchical Self-Organizing Maps. J Atmos Ocean Technol 23(2):325–338

Liu Y, Weisberg RH, Mooers CNK (2006b) Performance evaluation of the self-organizing map for feature extraction. J Geophys Res 111:C05018. https://doi.org/10.1029/2005JC003117

Liu Z et al (2018) Evaluation of spatial and temporal performances of ERA-Interim precipitation and temperature in mainland China. J Clim 31(11):4347–4365

Luo D (2005) Why is the North Atlantic block more frequent and long-lived during the negative NAO phase? Geophys Res Lett 32:L20804

Luo D, Gong T (2006) A possible mechanism for the eastward shift of interannual NAO action centers in last three decades. Geophys Res Lett 33(24):L24815. https://doi.org/10.1029/2006gl027860

Luo D, Diao Y, Feldstein S (2011) The variability of the Atlantic storm track and North Atlantic Oscillations: a link between intraseasonal and interannual variability. J Atmos Sci 68(3):577–611

Luo D, Cha J, Zhong L, Dai A (2014) A nonlinear multiscale interaction model for atmospheric blocking: the eddy-blocking matching mechanism. Q J R Meteorol Soc 140(683):1785–1808

Luo D, Chen X, Dai A, Simmonds I (2018) Changes in atmospheric blocking circulations linked with winter Arctic warming: a new perspective. J Clim 31(18):7661–7678. https://doi.org/10.1175/jcli-d-18-0040.1

Ma S, Zhou T, Stone DA, Polson D, Dai A, Stott PA, von Storch H, Qian Y, Burke C, Wu P, Zou L, Ciavarella A (2017) Detectable anthropogenic shift toward heavy precipitation over Eastern China. J Clim 30:1381–1396. https://doi.org/10.1175/JCLI-D-16-0311.1

Martinez JA, Dominguez F (2014) Sources of atmospheric moisture for the La Plata river basin. J Clim 27:6737–6753. https://doi.org/10.1175/JCLI-D-14-00022.1

Numaguti A (1999) Origin and recycling processes of precipitation water over the Eurasian continent: experiments using an atmospheric general circulation model. J Geophys Res 104:1957–1972

Park D, Lee S, Feldstein S (2015) Attribution of the recent winter sea ice decline over the Atlantic sector of the Arctic Ocean. J Clim 28:4027–4033. https://doi.org/10.1175/JCLI-D-15-0042.1

Quenouille M (1952) Associated measurements. Butterworths, London, pp 359–381

Risien CM, Reason CJC, Shillington FA, Chelton DB (2004) Variability in satellite winds over the Benguela upwelling system during 1999–2000. J Geophys Res 109:C03010. https://doi.org/10.1029/2003JC001880

Schneider U, Becker A, Finger P, Meyer-Christoffer A, Rudolf B, Ziese M (2015) GPCC Full Data Monthly Product Version 7.0 at 1.0: monthly land-surface precipitation from rain-gauges built on GTS-based and historic data. https://doi.org/10.5676/dwd_gpcc/fd_m_v7_100

Si D, Ding Y (2013) Decadal change in the correlation pattern between the Tibetan Plateau winter snow and the east Asian summer precipitation during 1970–2011. J Clim 26:7622–7634. https://doi.org/10.1175/JCLI-D-12-00587.1

Si D, Ding Y, Liu Y (2009) Decadal northward shift of the Meiyu belt and the possible cause. Chin Sci Bull 54:4742–4748

Simmonds I, Bi D, Yan B (1996) Relationships between summer rainfall over China and ocean temperatures in the Tropical Western Pacific. J Meteorol Soc Jpn Ser II 74(2):273–279

Simmonds I, Bi D, Hope P (1999) Atmospheric water vapor flux and its association with rainfall over China in summer. J Clim 12(5):1353–1367

Sodemann H, Stohl A (2009) Asymmetries in the moisture origin of Antarctic precipitation. Geophys Res Lett 36:L22803

Sodemann H, Schwierz C, Wernli H (2008) Interannual variability of Greenland winter precipitation sources: Lagrangian moisture diagnostic and North Atlantic Oscillation influence. J Geophys Res 113:D03107. https://doi.org/10.1029/2007JD008503

Stohl A, James P (2004) A Lagrangian analysis of the atmospheric branch of the global water cycle. Part I: method description, validation, and demonstration for the August 2002 flooding in Central Europe. J Hydrometeorol 5:656–678

Su T, Feng T, Feng G (2015) Evaporation variability under climate warming in five reanalyses and its association with pan evaporation over China. J Geophys Res Atmos 120(16):8080–8098

Sun J, Wang H (2012) Changes of the connection between the summer North Atlantic Oscillation and the East Asian summer rainfall. J Geophys Res 117:D08110. https://doi.org/10.1029/2012JD017482

Trenberth K, Fasullo JT, Mackaro J (2011) Atmospheric moisture transports from ocean to land and global energy flows in reanalyses. J Clim 24:4907–4924. https://doi.org/10.1175/2011JCLI4171.1

van der Ent RJ, Savenije HHG, Schaefli B, Steele-Dunne SC (2010) Origina and fate of atmospheric moisture over continents. Water Resour Res 46:W09525. https://doi.org/10.1029/2010WR009127

Vesanto J, Himberg J, Alhoniemi E, Parhankangas J (2000) SOM Toolbox for Matlab 5, Report. Helsinki University of Technology, Helsinki

Wang H (2001) The weakening of the Asian monsoon circulation after then end of 1970's. Adv Atmos Sci 18:376–386

Wang H (2002) Instability of the East Asian summer monsoon-ENSO relations. Adv Atmos Sci 19:1–11. https://doi.org/10.1007/s00376-002-0029-5

Wang K, Dickinson RE (2012) A review of global terrestrial evapotranspiration: observation, modeling, climatology, and climatic variability. Rev Geophys 50:RG2005. https://doi.org/10.1029/2011rg000373

Wang M, Paegle J (1996) Impact of analysis uncertainty upon regional atmospheric moisture flux. J Geophys Res Atmos 101(D3):7291–7303

Wang H, Xue F (2003) Interannual variability of Somali jet and its influences on the inter-hemispheric water vapor transport and on the East Asian summer rainfall. Chin J Geophys 46:11–20

Wei J, Dirmeyer PA, Bosilovich MG, Wu R (2012) Water vapor sources for Yangtze river valley rainfall: climatology, variability, and implications for rainfall forecasting. J Geophys Res 117:D05126. https://doi.org/10.1029/2011JD016902

Wu B, Zhang R, Wang B, D'Arrigo R (2009) On the association between spring Arctic sea ice concentration and Chinese summer rainfall. Geophys Res Lett 36:L09501. https://doi.org/10.1029/2009GL037299

Wu R, Wen Z, Yang S, Li Y (2010) An interdecadal change in Southern China summer rainfall around 1992/93. J Clim 23:2389–2403. https://doi.org/10.1175/2009jcli3336.1

Yao C, Yang S, Qian W, Lin Z, Wen M (2008) Regional summer precipitation events in Asia and their changes in the past decades. J Geophys Res 113:D17107. https://doi.org/10.1029/2007JD009603

Yu J, Lu M, Kim S (2012) A change in the relationship between tropical central Pacific SST variability and the extratropical atmosphere around 1990. Environ Res Lett 7:034025. https://doi.org/10.1088/1748-9326/7/3/034025

Zhang L, Zhou T (2015) Drought over east Asia: a review. J Clim 28:3375–3399. https://doi.org/10.1175/JCLI-D-14-00259.1

Zhou T, Yu R (2005) Atmospheric water vapor transport associated with typical anomalous summer rainfall patterns in China. J Geophys Res 110:D08104. https://doi.org/10.1029/2004JD005413

Zhou X, Ding Y, Wang P (2008) Moisture transport in the Asian summer monsoon region and its relationship with summer precipitation in China. Acta Meteorol Sin 24(1):31–42 **(in Chinese)**

Zhou T, Gong D, Li J, Li B (2009) Detecting and understanding the multi-decadal variability of the east Asian summer monsoon—recent progress and state of affairs. Meteorol Z 18(4):455–467

Zou L, Zhou T, Li L, Zhang J (2010) East China summer rainfall variability of 1958–2000: dynamical downscaling with a variable-resolution AGCM. J Clim 23:6394–6408. https://doi.org/10.1175/2010JCLI3689.1